Journal Pre-proof

Zinc Oxide Nanowires: Hydrothermal Synthesis, and Structural, Electrical, and Piezoelectric Characterizations

Imen Ben khaled, Elhadj Dogheche, Philippe Leclère

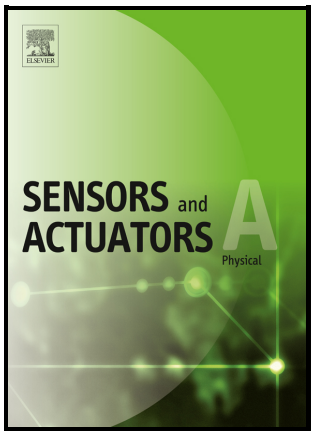

PII: S0924-4247(26)00298-0

DOI: https://doi.org/10.1016/j.sna.2026.117747

Reference: SNA117747

To appear in: *Sensors and Actuators: A. Physical*

Received date: 2 December 2025
Revised date: 17 March 2026
Accepted date: 18 March 2026

Please cite this article as: Imen Ben khaled, Elhadj Dogheche and Philippe Leclère, Zinc Oxide Nanowires: Hydrothermal Synthesis, and Structural, Electrical, and Piezoelectric Characterizations, *Sensors and Actuators: A. Physical,* (2026) doi:https://doi.org/10.1016/j.sna.2026.117747

Zinc Oxide Nanowires: Hydrothermal Synthesis, and Structural, Electrical, and Piezoelectric Characterizations

Imen Ben khaled [a,b], Elhadj Dogheche[b] and Philippe Leclère[a*]
[a] Laboratory for Physics of Nanomaterials and Energy (LPNE), Research Institute in Materials Science and Engineering, University of Mons (UMONS), B-7000 Mons, Belgium.
[b] Institut d'Electronique, Microélectronique et Nanotechnologie (IEMN) UMR CNRS 8520, Université Polytechnique Hauts de France (UPHF), F – 59300 Valenciennes, France.

Email: benkhaledimen123@gmail.com, philippe.leclere@umons.ac.be

Abstract.

Zinc oxide (ZnO) nanowires (NWs) are attractive lead-free piezoelectric nanomaterials with wide range of applications. In this work, vertically aligned ZnO NWs were synthesized on sputtered ZnO seed layers via a hydrothermal process. We investigated the effects of seed layer and NWs synthesis duration on the structural, morphological, electrical, and piezoelectric properties of the NWs. all measurements were repeated on multiple samples prepared under identical conditions. The argon/oxygen gas flow ratio during sputtering of the seed layer was optimized at (80:20)%, yielding high-quality ZnO seed layer with strong c-axis orientation and smooth surface morphology, stable structural features were consistently observed. A 240 nm seed layer was identified as the minimum thickness providing excellent grain coalescence and vertical NWs alignment. Hydrothermal synthesis times ranging from 1 h to 24 h revealed that the length of NWs increased, while their diameter showed rapid enlargement during the first 4 h, followed by saturation after 14 h. Optimally synthesized NWs (14 h on a 240 nm-thick seed layer) exhibit well-aligned arrays with hexagonal faces. Energy-dispersive X-ray spectroscopy (EDS) confirmed an almost stoichiometric ZnO composition with minimal impurities indicating a good chemical stability of the synthesis process. Nanoscale electrical measurements (conductive AFM) showed that integrating NWs on the seed layer enhanced current flow and the turn-on voltage, attributable to improved surface-to-volume ratio and charge transport in the NWs, consistent I–V characteristics were obtained at different locations and over repeated measurements, confirming measurement reliability. Piezoelectric force microscopy (PFM) measurements repeated at different NWs and at different positions under identical conditions revealed an effective piezoelectric coefficient of ~15 pm/V, about three times higher than that of the equivalent ZnO layer (~5.2 pm/V). These results demonstrate the essential role of the seed layer in enabling the growth of high-performance ZnO nanowires with reproducible, stable, and reliable structural, electrical, and piezoelectric properties.

Keywords

ZnO, piezoelectric, semiconductor, NWs, Hydrothermal synthesis, Sputtering, Lead free, Energy, Seed layer, AFM, C-AFM, PFM.

1. Introduction

Zinc oxide (ZnO) is a II–VI semiconductor that intrinsically exhibits piezoelectric properties [1], making it a highly promising and environmentally friendly alternative to lead-based materials used in advanced electronic and optoelectronic devices, particularly in view of the growing interest in mechanical energy harvesting applications [2]. In this context, there is an increasing need to promote so-called green materials, which combine natural abundance, low toxicity, economic affordability, and versatility in terms of physical and chemical properties, thereby enabling sustainable technological development without adverse effects on the environment. Unlike lead-based materials such as lead zirconate titanate (PZT), ZnO is lead-free, which aligns with the growing demand for sustainable, non-toxic materials. From a crystallographic point of view, ZnO crystallizes in the hexagonal wurtzite-type structure, which represents its most thermodynamically stable phase under ambient conditions. This crystal structure is characterized by a non-centrosymmetric arrangement of atoms, a key feature that underlies its piezoelectric behaviour. In terms of electronic properties, ZnO exhibits a wide direct bandgap of approximately 3.37 eV at room temperature and a high exciton binding energy (~60 meV), which promotes efficient optoelectronic performance [3].

Owing to its outstanding optical, electrical, mechanical, and piezoelectric characteristics, ZnO has attracted significant research interest because it can be synthesized into a wide variety of nanostructured forms, including nanowires, nanorods, nanoflowers, and nanoparticles, each offering specific surface areas and aspect ratios that can be exploited for specific functionalities [4]. Among these morphologies, ZnO NWs stand out due to their high aspect ratio, directional growth, and adjustable dimensions, which make them exceptionally well suited for diverse applications such as solar cells [5], [6] where ZnO NWs function as efficient charge collectors and light-scattering elements, gas sensors [7], [8] for the detection of pollutant gases, and piezoelectric nanogenerators [9], [10] where ZnO NWs convert mechanical vibrations into electrical energy. Additionally, ZnO NWs are integrated into UV light-emitting diodes [11], field-effect transistors [12], and photocatalytic applications [13].

Several fabrication techniques have been developed for the synthesis of ZnO NWs, including vapor–liquid–solid (VLS) growth [14], metal–organic chemical vapor deposition (MOCVD) [15], spray pyrolysis [16], pulsed laser deposition (PLD) [17], [18], and chemical bath deposition (CBD) [19], [20]. However, hydrothermal synthesis [10], [21], [22], [23], [24] has emerged as a method of choice for growing ZnO NWs due to its simplicity, low cost, and minimal environmental impact compared to high-temperature or vacuum-based techniques [25], [26]. Unlike methods that require complex equipment and high temperatures, hydrothermal synthesis can be carried out in aqueous solutions under relatively mild conditions. This makes the process not only energy-efficient, but also compatible with large-scale production. One of the main advantages of this approach is its ability to grow vertically aligned NWs at relatively low temperatures, typically below 120 °C, making it compatible with various substrates [27].

A critical aspect of ZnO NWs synthesis lies in the use of a seed layer. This seed layer, often deposited by techniques such as sputtering [19], sol–gel methods [20] or spin coating methods [23],

provides nucleation sites that guide the vertical growth of the NWs. Its presence promotes heterogeneous nucleation, leading to a significant improvement in the crystallinity of the resulting nanowires and controls their density and diameter [28], [29], [30], [31] . The microstructural characteristics of the seed layer, in particular its texture and thickness, significantly influence the orientation and uniformity of the NWs, playing a decisive role in obtaining high-quality aligned structures [32], [33].

By fine-tuning these parameters, researchers can engineer high-quality, highly aligned ZnO NWs arrays that exhibit superior performance in optoelectronic, sensing, and energy-harvesting applications.

In this study, ZnO nanowires were synthesized by a low-temperature hydrothermal process on ZnO seed layers deposited via RF magnetron sputtering on silicon substrates. We focused on optimizing the seed layer by investigating the influence of the $Ar:O_2$ gas flow ratio during seed layer deposition. We also studied the thickness of the seed layer and its impact on the nanowires. Furthermore, we optimized the hydrothermal synthesis of NWs by varying the synthesis time. The synthesized nanostructures were subjected to structural, morphological, electrical, and piezoelectric characterizations.

2. Materials and Methods

2.1. Materials

For the preparation of the ZnO seed layer, high-purity zinc oxide powder (ZnO, 99.99%) was sourced from NEYCO Vacuum and Materials. For hydrothermal synthesis, zinc nitrate hexahydrate ($Zn(NO_3)_2 \cdot 6H_2O$, 98%) was also obtained from NEYCO, and hexamethylenetetramine (HMTA, ≥99.5%) was sourced from Sigma-Aldrich. When dissolved in distilled water, zinc nitrate hexahydrate releases Zn^{2+} ions that are essential for growing the ZnO nanowires, and HMTA releases hydroxide ions (OH^-). Zn^{2+} and OH^- react to form ZnO.

2.2. Methods

The entire study was carried out using n-type silicon wafers with a thickness of 380 µm and a crystallographic orientation of (100). Before any deposition or growth process, the silicon substrates underwent a rigorous cleaning procedure to remove surface contaminants that could interfere with the adhesion and uniformity of the seed layer. They were immersed in acetone, ethanol, and distilled water for 10 min each and were subjected to ultrasonic agitation. After solvent cleaning, the silicon wafers were dried under nitrogen gas.

2.2.1. ZnO seed layer deposition

The ZnO seed layers were deposited at room temperature using an RF magnetron sputtering system (PLASSYS MP600). The substrate temperature was considered stable during deposition, and no temperature control system was employed to regulate or stabilize the temperature. The silicon substrates were mounted at a fixed distance of 8 cm, positioned parallel to the target surface. The homemade ceramic ZnO target used for sputtering had a 3-inch diameter and was fabricated by first drying 18.5 g of high-purity ZnO powder (99.99%) in an oven at 100 °C, then pressing it under 20 tons of pressure; the target was not sintered. During deposition, the working atmosphere was a mixture of argon and oxygen, with a ratio ($Ar:O_2$) varying between pure Ar (100:0), (90:10)%, (80:20)%, and (70:30)%. This variation in gas composition allowed us to optimize the

stoichiometry and crystallinity of the obtained ZnO seed layer. The sputtering pressure was set at 15 mTorr, which was found to be optimal; higher pressures caused plasma instability and a significant increase in reflected power. The sputtered power was maintained at 40 W, which proved to be optimal for our homemade target; increasing the power beyond this value caused the formation of cracks in the target, affecting the quality of the deposited seed layer. This careful control of deposition parameters, non-sintered target usage, gas ratio, substrate positioning, sputtering pressure, power and ambient temperature deposition was essential to obtain uniform, high-quality ZnO seed layers, which play a crucial role in the synthesis of well-aligned ZnO nanowires.

2.2.2. Synthesis of ZnO NWs

For the synthesis of ZnO NWs, an aqueous precursor solution was prepared using zinc nitrate hexahydrate ($Zn(NO_3)_2 \cdot 6H_2O$) and hexamethylenetetramine (HMTA) at equimolar concentrations [31]. Specifically, 1.8 g of $Zn(NO_3)_2 \cdot 6H_2O$ was dissolved in 60 mL of distilled water and stirred for 15 min in a first beaker, while 0.9 g of HMTA was dissolved in 60 mL of distilled water and stirred for 15 min in a second beaker to ensure complete dissolution. The two precursor solutions were then mixed together and transferred into a Teflon container, which was filled to 50 % of its volume with the final solution. The mixed solution was further stirred for 30 min to guarantee homogeneity and to prevent premature precipitation.

Subsequently, the substrates coated with ZnO seed layers were immersed in the solution, and the hydrothermal synthesis was carried out at 90 °C with a heating rate of 2 °C min^{-1}, ensuring controlled and reproducible growth conditions. Synthesis durations of 1 h, 4 h, 14 h, and 24 h were investigated to study the evolution of nanowire length, diameter, and density as a function of growth time. After synthesis, the samples were removed from the solution, thoroughly rinsed three times with distilled water to eliminate residual salts without ultrasonic assistance, since ultrasonic cleaning may detach the NWs, and finally dried under a gentle nitrogen flow.

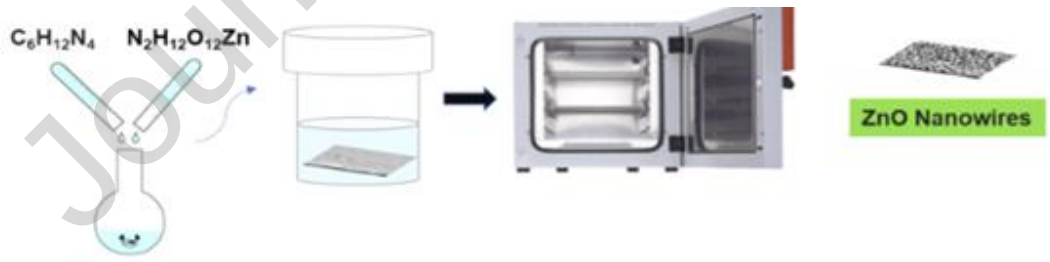

Figure 1: Schematic illustration of ZnO NWs array synthesis. [31]

3. Characterizations

3.1. Structural and morphological properties

The resulting ZnO seed layers and NWs were characterized using several complementary techniques to assess their structural and morphological properties. X-ray diffraction (XRD) measurements were carried out with a Siemens D5000 diffractometer equipped with Cu Kα radiation (λ = 1.5406 Å), operating at an accelerating voltage of 40 kV and a current of 40 mA. These measurements provided information on the crystallinity and preferred orientation of both the seed layers and the hydrothermally synthesized NWs. The diffraction angle 2θ was determined

from the maximum intensity position of the corresponding XRD peak, while the full width at half maximum (FWHM) was extracted from the peak width measured at half of the maximum intensity. The surface topography of the ZnO seed layers and NWs was investigated using atomic force microscopy (AFM, Bruker Dimension ICON). This high-resolution technique provided an accurate imaging of the nanometric features and surface roughness. Measurements were performed in contact mode, in which the AFM tip remains in constant contact with the surface during scanning, allowing for accurate mapping of fine surface details. To further study the morphology, a Thermo Scientific Quattro Environmental Scanning Electron Microscope (SEM) was employed. For all samples, SEM imaging was conducted in high-vacuum mode at 20 kV with a spot size of 3 µm, providing clear and detailed images of the nanostructures. Cross-sectional SEM images were used to determine the length and vertical alignment of the ZnO NWs, while top-view images were analysed to extract the average diameter and surface density of both the seeds and NWs using Mountains software. To further confirm the elemental composition and purity of the ZnO NWs, energy-dispersive X-ray spectroscopy (EDS) was performed.

3.2. Electrical properties

The electrical properties of ZnO seed layers and nanowires were investigated at the nanoscale using a conductive atomic force microscopy (C-AFM). This AFM mode is specifically designed to probe local electrical conductivity using a Pt/Ir-coated conductive tip (SCM-PIT V2), which ensures both mechanical durability and stable electrical contact during scanning. During C-AFM measurements, the tip is brought into contact with the sample surface under a constant force of 70 nN, while a DC bias voltage was applied. This contact force was carefully chosen as it provides stable and reproducible electrical measurements over extended periods and across different samples, different locations on the same sample, and repeated scans, without inducing mechanical damage to the nanostructures.

For imaging and positioning, the tip scanning hold time was set to 50 ms, ensuring reliable current mapping while minimizing tip-induced artifacts. Current–voltage (I–V) characteristics were acquired by holding the tip at a fixed position and ramping the applied bias with a voltage step of 0.1 V, allowing accurate extraction of local electrical properties.

This approach allows the study of local conduction mechanisms, barrier heights, and defect-related transport phenomena at specific grains or individual nanowires. This technique offers high current sensitivity that characterizes conductivity variations across medium to low conducting and semiconducting materials. It enables characterization of ultra-low currents in the 2 pA to 1 µA range.

To ensure statistical relevance, I–V measurements on ZnO nanowires were repeated on approximately ten individual nanowires within a scanned area of 1 x 1 µm². For each nanowire, the measurement was performed five times: once at the centre of the nanowire and four times on its lateral sides. This measurement protocol allows assessment of both intra-nanowire and inter-nanowire electrical variability.

3.3. Piezoelectric properties

The piezoelectric properties of ZnO seed layer and nanowires were evaluated by determining the effective piezoelectric coefficient $d_{33,eff}$. This coefficient, expressed in pm/V or pC/N, quantifies a material's ability to deform along the vertical axis (z) under the effect of an applied electric field

or, conversely, to generate an electric signal when subjected to a mechanical stress in the same direction. A higher $d_{33,eff}$ value directly indicates a stronger piezoelectric response, which is essential for applications such as nanogenerators, sensors, and actuators. In order to study these properties at the nanoscale, Piezoresponse force microscopy (PFM) measurements were performed using an atomic force microscope (AFM, Bruker Dimension ICON) equipped with a Pt/Ir-coated conductive tip (SCM-PIT V2). In PFM, a small AC voltage is applied between the conductive probe and the sample while the tip remains in contact with the surface. This voltage induces mechanical deformations in the sample through the inverse piezoelectric effect, causing vertical displacements that are detected by the AFM cantilever. The amplitude of this displacement, normalized by the applied AC voltage, gives the effective piezoelectric response ($d_{33,eff}$) [34]:

$$d_{33,eff}=\frac{Displacement}{V_{AC}} \quad (1)$$

Prior to these measurements, system calibration was performed. Calibration of the AFM tip is essential to determine its deflection sensitivity (approximately 90 nm/V for the SCM-PIT V2 tip). Before starting measurements, the laser spot was aligned at the electrostatic blind spot (ESBS) to minimize electrostatic contributions. Next, a reference sample (PZT) was used to measure the cantilever's resonance frequency and phase (φ) to determine the phase offset (φ_offset) needed to ensure the PFM phase of the oriented domain follows $\frac{\pi}{2}$ or $-\frac{\pi}{2}$. The PZT used for calibration has a piezoelectric coefficient d_{33} = 60 pm/V.

The piezoelectric coefficient d_{33},eff was calculated by applying an AC voltage near the cantilever's contact resonance frequency (f_r=310 kHz), providing accurate measurements of the amplitude (A), phase (φ), and quality factor (Q) of the resonance to enable quantification of the effective piezoelectric response. The detected amplitude signal (A) is amplified by a quality factor Q while operating at the contact resonance**;** this requires taking it into consideration in the displacement response (in pm):

$$Displacement = \frac{A}{Q} sin\,(\varphi) \quad (2)$$

A conductive tip with a 25 nm radius was used in contact mode on top of the ZnO seed layer and NWs. After establishing the contact resonance and applying a controlled constant force of 70 nN between the tip and the samples, displacement values were recorded by sweeping the AC voltage between 100 mV and 2 V. The d_{33},eff values were then determined by calculating the slope of displacement as a function of AC voltage.

4. Results and discussion

4.1. Seed layer optimization

4.1.1. XRD Analysis

Figure 2a shows the XRD patterns of ZnO seed layers deposited under different Ar:O_2 flow ratios, and the corresponding 2θ peak positions and FWHM values plotted as functions of the Ar:O_2 flow ratio. All the seed layers exhibit only a dominant diffraction peak corresponding to the (002) crystallographic plane of ZnO, with 2θ values ranging between ~34.20 ± 0.04° for pure Ar and 34.62 ± 0.02° for Ar:O2 of (80:20)%, confirming the formation of a hexagonal wurtzite structure with a strong preferential orientation along the c-axis, without additional peaks, a desirable feature for piezoelectric applications.

As depicted in Figure 2b, the position of the (002) peak shifts with the gas composition. Starting from 34.20° under pure Ar atmosphere, it gradually shifts to 34.62° for an (80:20)% Ar:O_2 mixture, before slightly decreasing again at (70:30)% Ar:O_2. This total shift of about 0.4° reflects modifications of the lattice parameters along the *c*-axis, indicating the presence of residual stress within the ZnO crystalline lattice. The shift of the diffraction peak toward higher 2θ values suggests a reduction in the interplanar spacing d_{002}, associated with the development of compressive stress as oxygen incorporation increases. These variations are most likely related to changes in oxygen stoichiometry and defect concentration, particularly oxygen vacancies, which are known to induce lattice distortions in ZnO. Consequently, a moderate oxygen supply contributes to improved crystalline ordering, in good agreement with previous reports. [35]

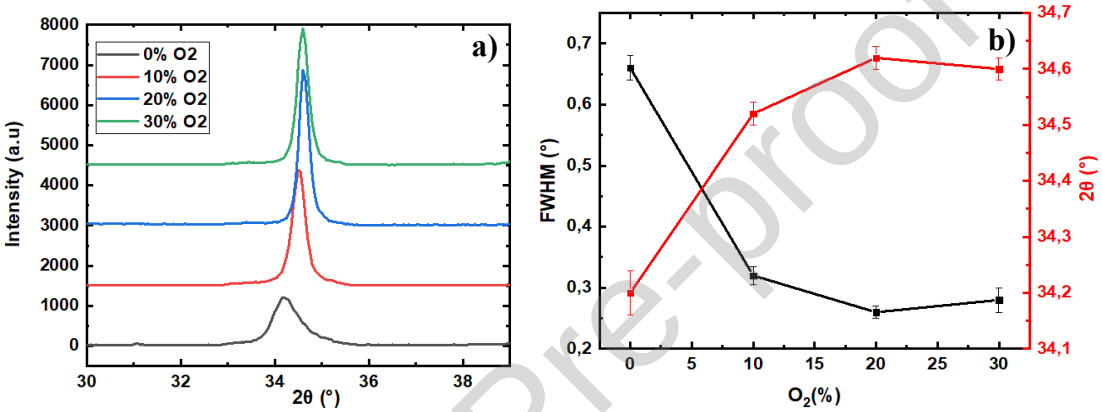

Figure 2: (a) XRD patterns of seed layers at different Ar:O_2 flow ratios, (b) 2θ and FWHM as functions of the Ar:O_2 flow ratio. The solid lines connecting the data points in figure 2b are only guides to the eye.

In addition to peak position, the full width at half maximum (FWHM) of the (002) peak, also shown in Figure 2b, provides insight into the crystalline coherence and grain size. A narrower FWHM indicates better crystalline quality. The FWHM decreases with increasing oxygen content up to the (80:20)% Ar:O_2, reaching a minimum of 0.260 ± 0.001°. This result highlights the formation of a highly oriented and well-textured ZnO layer. At (70:30)% Ar:O_2, the FWHM increases slightly, likely due to excessive oxygen incorporation leading to increased defect formation.

The average crystallite size (D) was estimated from the (002) peak using the Scherrer equation:

$$D = \frac{K\lambda}{\beta cos\theta} \quad (3)$$

where $D$is the crystallite size (nm), $K$is the shape factor (typically ≈ 0.9), $\lambda$is the X-ray wavelength (e.g. Cu K_α = 1.5406 Å), β is the full width at half maximum (FWHM) of the diffraction peak, and θ is the Bragg angle.

The calculated crystallite sizes increase from approximately 12.5 nm for pure Ar to about 25.1 nm for (90:10)% Ar:O_2, 30.9 nm for (80:20)% Ar:O_2, and 28.7 nm for (70:30)% Ar:O_2. These values are fully consistent with the literature, where the crystallite size of ZnO thin films typically ranges from about 5 nm to over 33 nm [36], [37], [38], [39] depending strongly on the deposition technique, annealing temperature, and substrate nature. The inverse correlation between FWHM and crystallite size observed here clearly reflects an improvement in crystalline quality, associated

with reduced micro-strain and defect density. Conversely, the smaller crystallite size obtained under pure Ar conditions indicates a lower degree of crystalline order.

Overall, these results demonstrate that the (80:20)% Ar:O_2 flow ratio provides an optimal balance between sputtering efficiency and oxygen availability, leading to highly oriented, well-crystallized ZnO seed layers. Such structural quality is particularly favorable for the subsequent growth of vertically aligned ZnO nanowires.

4.1.2. Topological properties

Figure 3 presents the surface topography of ZnO seed layers deposited under various Ar:O_2 flow ratios, as characterized by AFM. Across all samples, a similar surface morphology is observed, namely a rough, domed structure. This texture aligns well with the Structure Zone Model (SZM), particularly Thornton's model [40], which correlates deposition parameters (especially the ratio of substrate temperature T_s to the melting point of the target material T_m) with the resulting seed layer microstructure.

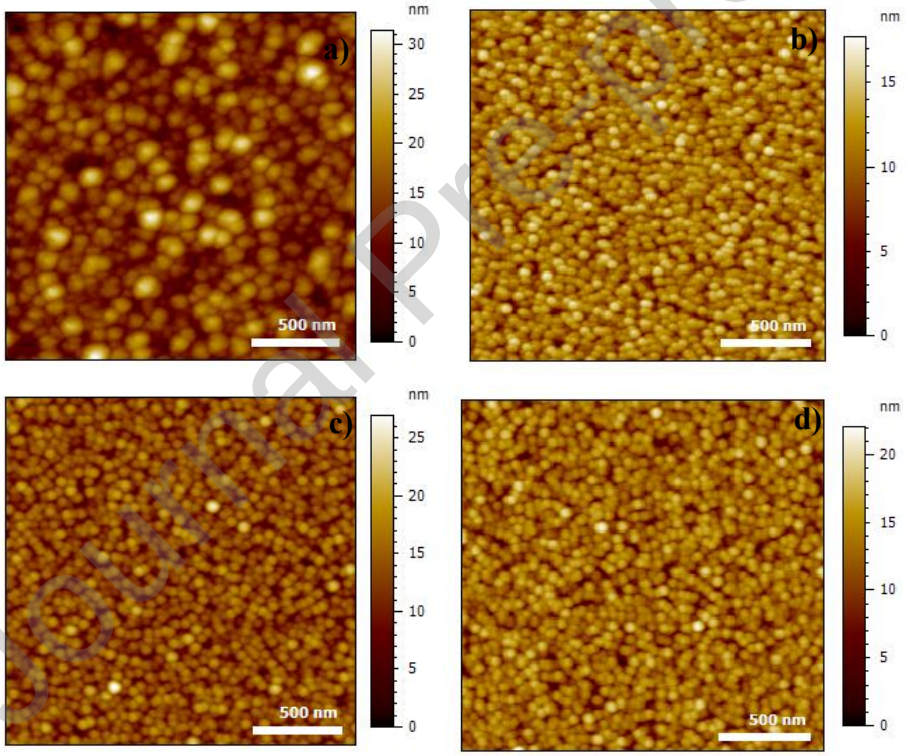

Figure 3: Surface topographies of ZnO seed layers deposited under (a) pure Ar, (b) (90:10)%, (c) (80:20)%, and (d) (70:30)% Ar:O_2.

Given the substrate temperature used in this study (room temperature) and the high melting point of ZnO ($T_m \approx 1975$ °C), the condition $T_s/T_m < 0.3$ places the growth regime within Zone 1 of the SZM. This zone leads to the formation of a columnar structure with rough, domed surfaces separated by intercolumnar voids [40]. This morphology is particularly relevant for NWs growth, as surface roughness and grains (called also seeds) can influence nucleation density and alignment.

Figure 4 shows the variation in average surface roughness (R_a) as a function of the Ar:O_2 gas ratio. The bare silicon substrate exhibits a smooth surface ($R_a \approx 0.5$ nm). The AFM measurements were

performed over a scanning area of 2 × 2 µm². To ensure data representativeness, the surface roughness was analysed over several distinct regions of identical size (2 × 2 µm²), and comparable R_a values were obtained, indicating a good homogeneity of the surface roughness across the sample. Upon ZnO deposition, roughness increases due to the formation of crystallites. The highest roughness (~3.51 ± 0.08 nm) is observed for the seed layer grown under pure Ar. When oxygen is introduced into the plasma, the roughness decreases significantly. The lowest R_a value (~2.60 ± 0.06 nm) is obtained with an Ar:O_2 ratio of (70:30)%, indicating that a moderate oxygen flow rate leads to more compact and uniform seed layers. Notably, in the intermediate ranges (90:10, 80:20, and 70:30)%, the variation in roughness is minimal (approximately ~0.2 nm), suggesting that oxygen levels above a certain threshold do not radically change the surface texture. These results highlight the critical role of plasma composition in adjusting surface morphology.

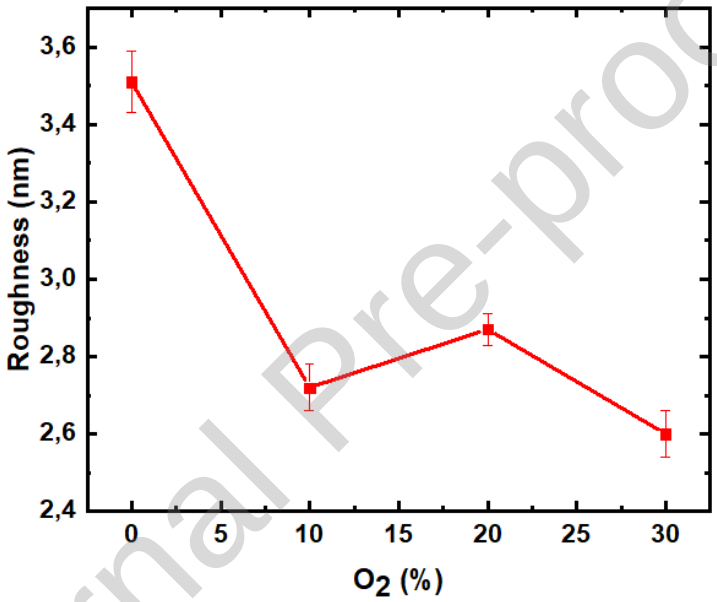

Figure 4: Evolution of seed layers roughness as a function of Ar:O_2 ratio. The solid lines connecting the data points are only guides to the eye.

4.1.3. Morphological properties

Figure 5 provides top-view SEM images of ZnO seed layers deposited under varying Ar:O_2 gas ratios, providing complementary morphological information to the AFM analysis. Consistent with AFM observations, all seed layers exhibit a rough, domed surface texture, typical of room-temperature sputtered ZnO films. However, the level of surface uniformity and grain distribution varies significantly with the gas composition during deposition.

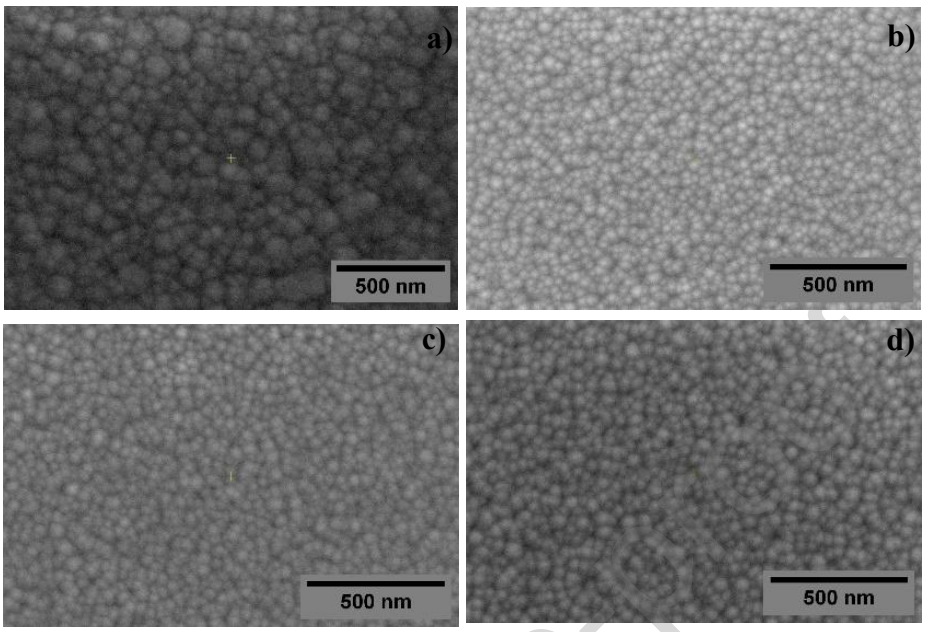

Figure 5: Top view SEM images of ZnO seed layers deposited under (a) pure Ar, (b) (90:10)%, (c) (80:20)%, and (d) (70:30)% Ar:O_2.

It should be noted that, seed layers deposited under Ar:O_2 mixtures have a more homogeneous granular structure than those grown in pure Ar, where larger and less uniform grains predominate. As reported in Table 1, the average grain size decreases significantly with the introduction of oxygen, from 86 ± 8 nm for pure Ar to 32 ± 2 nm for an Ar:O_2 ratio of (80:20)% [41]. This decrease in grain size is accompanied by a significant increase in particle density, from 120 ± 10 particles/µm² to 504 ± 15 particles/µm², as smaller grains allow for a higher packing density per unit area.

It is important to emphasize that the evolution of the grain size shows an inverse trend compared to the crystallite size estimated from XRD analysis. While the crystallite size reflects the dimension of coherently diffracting domains within the ZnO crystalline lattice, the grain size corresponds to the morphological entities observed at the surface, which may consist of one or several crystallites. In the case of deposition under pure Ar atmosphere, the crystallite size derived from the Scherrer analysis (≈ 12.5 nm) is much smaller than the grain size measured by microscopy (≈ 86 nm), indicating that each grain is composed of multiple crystallites. In particular, with increasing oxygen content, the crystallite size increases whereas the grain size decreases, and both tend to converge toward similar values, suggesting a reduction in internal grain subdivision and an improvement in crystalline coherence. Notably, for the (80:20)% Ar:O_2 condition, comparable grain and crystallite sizes are observed, indicating the formation of nearly single-crystalline grains with reduced defect density and enhanced structural uniformity.

Table 1: Mean grain size and density of ZnO seed layers deposited under pure Ar, (90:10)%, (80:20)%, and (70:30)% Ar:O_2.

Ar:O_2%	Mean Grain Size (nm)	Density (particles/μm²)
Pure Ar	86 ± 8	120 ± 10
(90:10)%	30 ± 3	532 ± 20
(80:20)%	32 ± 2	504 ± 15
(70:30)%	34 ± 2	501 ± 20

For seed layers deposited under Ar:O_2 gas ratios of (90:10)%, (80:20)%, and (70:30)%, the average grain size remained relatively stable, varying slightly between ~30 nm and ~34 nm. Similarly, the particle density showed only slight variations, fluctuating modestly between 501 and 532 particles/μm², despite the gradual increase in oxygen content. The microstructure appears to reach a near-equilibrium state in this range, indicating that moderate oxygen incorporation is sufficient to optimize grain refinement and uniformity without inducing significant morphological changes.

From these results, it is evident that ZnO seed layers grown under oxygen-containing atmospheres exhibit superior microstructural properties, characterized by smaller grain sizes, higher uniformity, and denser packing, all of which are beneficial for the growth of vertically aligned nanowires. In particular, the layer deposited with an (80:20)% Ar:O_2 ratio offers an optimal balance between crystallinity, surface uniformity and defect control, and was therefore selected as the reference seed layer for further hydrothermal ZnO NWs synthesis, to ensure improved alignment, density, and structural quality.

The Ar:O_2 gas ratio during deposition critically influences the stoichiometry and defect landscape of the seed layer. Higher oxygen content reduces oxygen vacancies, leading to a more stoichiometric lattice and slightly smaller lattice parameters, whereas oxygen-deficient conditions promote the formation of oxygen vacancies and zinc interstitials, locally expanding the lattice and affecting electronic and piezoelectric properties. By carefully controlling the oxygen ratio, it is possible to tune the lattice parameters, defect concentration, and internal stress, which in turn impacts nanowire nucleation, growth orientation, and overall crystallinity, ultimately enhancing the quality and performance of the resulting ZnO nanowires.

4.2. ZnO NWs synthesis

In order to synthesize well-aligned ZnO NWs with controlled diameter, uniform surface density, and improved crystallinity, a systematic study was conducted to evaluate the influence of hydrothermal synthesis duration and seed layer thickness. These two parameters are known to play a critical role in the vertical alignment, growth rate, and morphological uniformity of the resulting NWs. In this study, the ZnO seed layers were deposited under an optimized atmosphere (80:20)% Ar:O_2, a condition previously identified as promoting superior crystallographic orientation and surface homogeneity.

By fine, tuning the characteristics of the seed layer and adjusting the synthesis duration, we sought to optimize the architecture of the NWs for their subsequent integration into devices, particularly in piezoelectric applications.

4.2.1. Variation of synthesis time

4.2.1.1. XRD analysis

The crystallinity and preferred orientation of ZnO NWs synthesized for different durations (1 h, 4 h, 14 h, and 24 h) on a ~350 nm-thick ZnO seed layer deposited under an optimized atmosphere (80:20)% Ar:O_2 were evaluated by XRD, as shown in Figure 6a. For all samples, a dominant diffraction peak was observed between 2θ = 34.500 ± 0.008° for a 1 h synthesis and 34.700 ± 0.009° for a 24 h synthesis, corresponding to the (002) plane of the hexagonal wurtzite structure of ZnO. This indicates strong c-axis preferential growth. As the synthesis time increases, the intensity of the (002) peak becomes more pronounced, suggesting improved crystalline order and better vertical alignment of the nanowires.

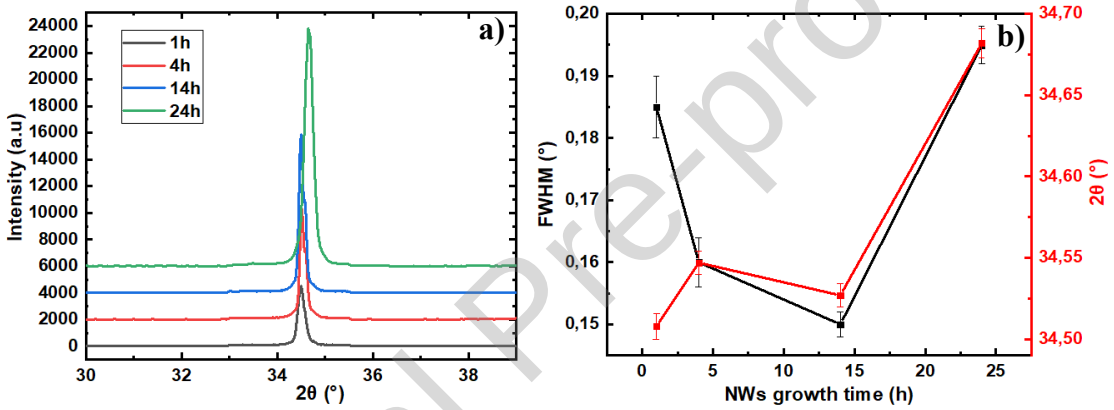

Figure 6: (a) XRD patterns of ZnO NWs synthesized for 1 h, 4 h, 14 h and 24 h on ZnO seed layers deposited under (80:20)% Ar:O_2, (b) 2θ and FWHM as functions of the synthesis time. The solid lines connecting the data points in figure 6b are only guides to the eye.

In Figure 6b, the variations in 2θ position and FWHM are plotted as a function of synthesis time. The results show a slight shift (~0.17°) in 2θ and a reduction in FWHM (~0.040° ± 0.002) with increasing synthesis time, indicating improved crystallinity. The smallest FWHM value, observed for NWs synthesized for 14 h, suggests an optimal balance between NWs growth, to elongate along a preferred crystal orientation and defect minimization, before defect accumulation starts.

A direct comparison between the ZnO seed layer (FWHM = 0.260 ± 0.001°) and the synthesized NWs (FWHM reduced to ~0.150 ± 0.002°) reveals that the NWs growth process further enhances crystal quality while preserving the (002) texturing. This improvement is primarily attributed to the high-quality seed layer [28], which promotes vertical alignment and coherent crystallographic orientation.

To assess the critical role of the seed layer, a control experiment was conducted by synthesizing ZnO NWs directly on bare silicon substrates under identical hydrothermal conditions (14 h synthesis). As illustrated in Figure 7, the resulting NWs exhibit a polycrystalline structure and markedly lower XRD peak intensities.

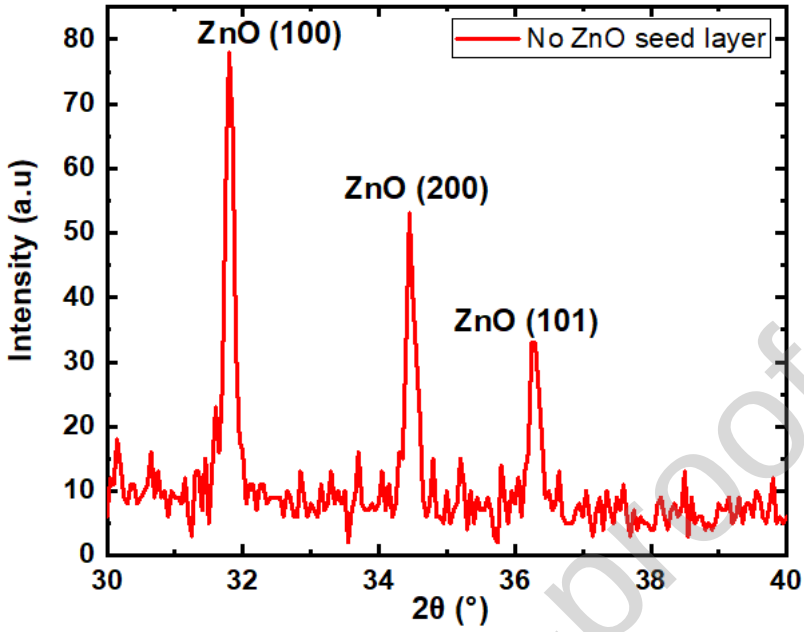

Figure 7: XRD patterns of ZnO NWs synthesized for 24h on a silicon substrate without ZnO seed layer.

This comparison clearly demonstrates that the presence of a high-quality seed layer is essential for ensuring crystallographic orientation and structural uniformity of NWs.

4.2.1.2. Morphological properties

Figure 8 presents top-view and cross-sectional SEM images of ZnO NWs synthesized on sputtered ZnO seed layers deposited under an optimized (80:20)% Ar:O_2 atmosphere. Four synthesis durations were investigated: 1 h, 4 h, 14 h, and 24 h. The top-view images of four different samples, for each composition, reveal that the NWs exhibit well-defined hexagonal faceted heads, characteristic of the wurtzite ZnO structure.

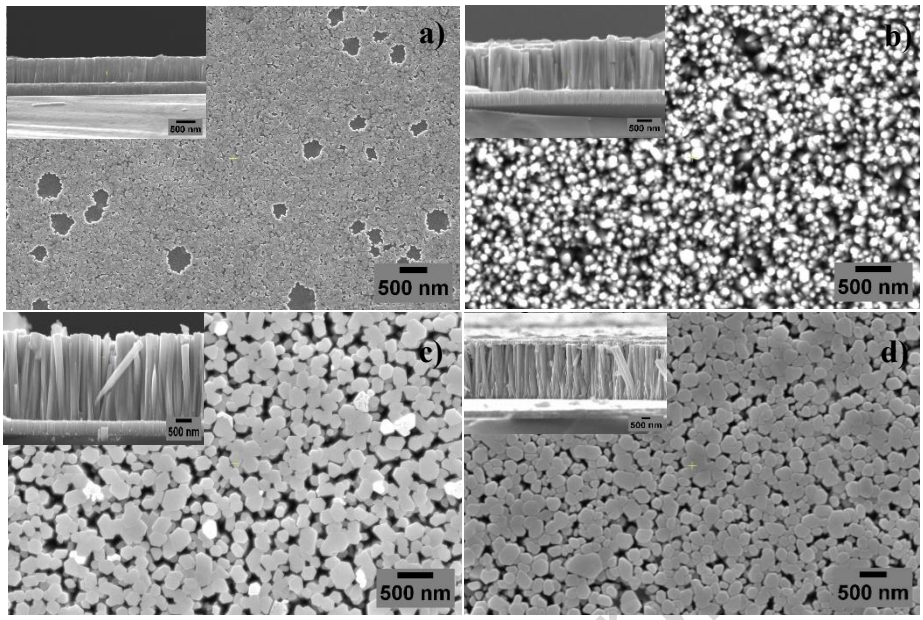

Figure 8: Top-view and cross-sectional SEM images of ZnO NWs synthesized for (a) 1 h, (b) 4 h, (c) 14 h, and (d) 24 h on ZnO seed layers deposited under (80:20)% Ar:O_2.

In Figure 8a, an incomplete coverage of the substrate by ZnO NWs is observed, characterized by the presence of regions devoid of growth. This behavior is mainly attributed to the limited hydrothermal synthesis time, which is 1 h in this case, and is insufficient to ensure adequate nucleation and growth for achieving a continuous surface coverage.

It is important to note that, for all samples, the hydrothermal synthesis was carried out on substrates with dimensions of 1 × 2 cm^2, and that this incomplete coverage is observed only for short synthesis durations (1 h). At this early stage of growth, NWs nucleation occurs preferentially on specific active sites of the seed layer, while other regions remain partially or completely inactive. This heterogeneous distribution may be related to local variations in seed density or crystallographic orientation, leading to non-uniform growth. When the synthesis time is increased, both the nucleation density and the nanowire length gradually increase, promoting lateral coalescence and resulting in an almost complete coverage of the substrate surface.

Table 2 summarizes the key morphological parameters, mean diameter, density, and mean length of the NWs at different synthesis times. Notably, over the first three synthesis durations (1 h, 4 h, and 14 h), there is a marked evolution in both average NWs diameter and density. The mean NWs diameter increases from ~31 ± 11 nm (1 h) to ~170 ± 4 nm (14 h), while the density decreases from ~888 ± 25 NWs/μm^2 to ~36 ± 5 NWs/μm^2, highlighting a coarsening mechanism where prolonged synthesis promotes lateral growth at the expense of density.

Interestingly, NWs synthesized for 24 h show morphological properties (diameter and density) comparable to those at 14 h [42], suggesting that lateral growth saturates after a critical time.

Table 2: Mean diameter, density, and length of ZnO NWs synthesized for 1 h, 4 h, 14 h, and 24 h on seed layers deposited at (80:20)% Ar:O_2.

Synthesis Duration	Mean NWs diameter (nm)	Density (NWs/µm²)	Mean NWs length (µm)
1 h	31 ± 11	888 ± 25	0.7 ± 0.1
4 h	94 ± 7	56 ± 10	1.60 ± 0.08
14 h	170 ± 4	36 ± 5	1.90 ± 0.06
24 h	172 ± 5	33 ± 7	2.50 ± 0.07

The cross-sectional SEM images in Figure 8 further reveal that the NWs maintain a high degree of vertical alignment throughout the different synthesis durations. The alignment and columnar growth are largely attributed to the seed layer. As shown in Table 2, the length of the NWs increases steadily with synthesis time, from approximately 0.7 ± 0.1 µm (1 h) to approximately 2.50 ± 0.07 µm (24 h). This indicates that axial growth continues even after lateral expansion slows, allowing the NWs to elongate while maintaining their orientation.

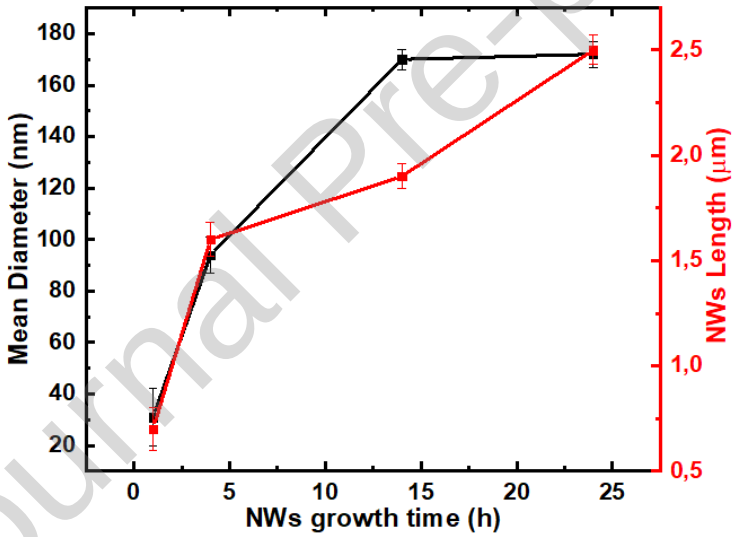

Figure 9: NWs mean diameter and length as a function of synthesis time. The solid lines connecting the data points are only guides to the eye.

As illustrated in Figure 9, the most significant changes in NWs morphology occur between 1 h and 4 h of synthesis, where both the mean diameter and length increase sharply. Beyond 4 h, the diameter evolution becomes more gradual, stabilizing after 14 h, while the length continues to increase, indicating a decoupling between axial and radial growth. After 14 h, the lateral growth of the nanowires stabilizes due to grain coalescence and surface energy minimization, while axial growth continues, where precursor diffusion and high surface energy promote continued elongation.

The sharp decline in NWs density during the early stages of growth is attributed to the rapid increase in NWs size, which limits the number of structures that can develop on a given surface area.

An important observation is that for the 1 h sample, the mean NWs diameter matches the average grain size of the seed layer, indicating a one-to-one correspondence between the nucleation sites and initial NWs. However, for longer synthesis durations (4 h, 14 h, 24 h), the NWs diameters exceed the original grain sizes [42], [43], implying that NWs grow not only vertically but also laterally, coalescing or expanding beyond the initial seed boundaries.

As illustrated in figure 10, top view SEM image of ZnO NWs synthesized for 14h on silicon substrate without seed layer showed disordered, randomly oriented NWs.

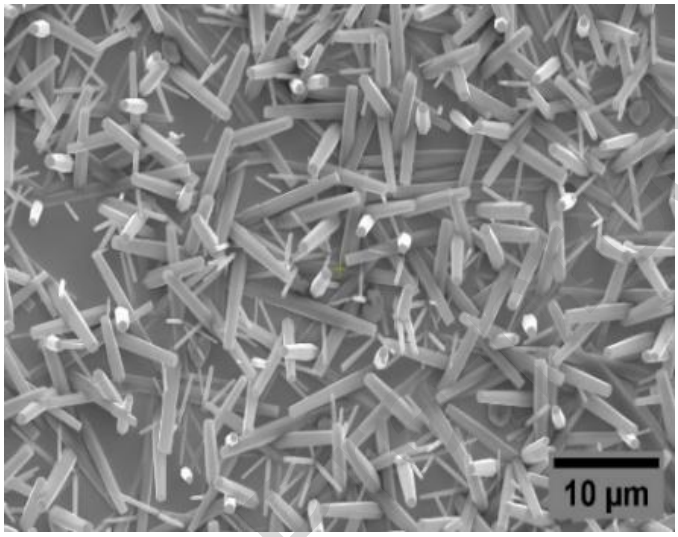

Figure 10: Top-view SEM image of ZnO NWs synthesized for 24h on a silicon substrate without ZnO seed layer.

Overall, these findings underscore the influence of the seed layer on the structural and morphological quality of ZnO NWs. An optimized seed layer not only improves crystallinity but also enables controlled and uniform growth, which is crucial for high-performance devices.

4.2.2. Effect of seed layer thickness

4.2.2.1. XRD Analysis

To investigate the influence of the seed layer thickness on the structural quality and morphology of ZnO NWs, seed layers were deposited by RF sputtering under an optimized (80:20)% Ar:O_2 atmosphere, with thicknesses varied between 80 nm, 125 nm, 240 nm, and 450 nm. ZnO NWs were then synthesized on top of these layers via hydrothermal synthesis for 14 h under identical conditions.

Figure 11 displays the XRD patterns of ZnO NWs synthesized on seed layers of different thicknesses.

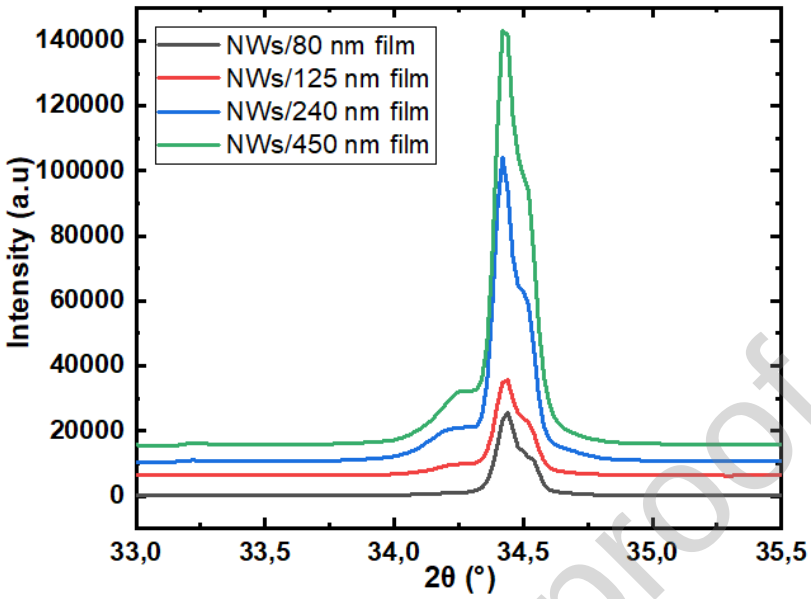

Figure 11: XRD patterns of ZnO NWs synthesized on seed layers of thickness: 80 nm, 125 nm, 240 nm and 450 nm.

For all samples, a dominant diffraction peak is observed at ~34.4°, corresponding to the (002) plane of the hexagonal wurtzite ZnO structure, indicating a strong preferential orientation along the c-axis. The increase in peak intensity and the presence of a narrower FWHM (~0.15°) for the NWs indicate a significant enhancement in crystallinity upon NWs growth. This improved crystallinity in the NWs suggests that the seed layer is indispensable, guiding both the orientation and the quality of the NWs during hydrothermal synthesis.

The shoulders observed on the diffraction peaks in Figure 11 correspond to the Kα components of the X-ray radiation used for the measurement.

In summary, increasing the seed layer thickness enhances the (002) peak intensity and promotes better crystalline quality in both the seed layers and the resulting ZnO NWs.

4.2.2.2. Morphological properties

Figure 12 presents SEM images of ZnO seed layers with varying thicknesses (80 nm, 125 nm, 240 nm, and 450 nm). All seed layers exhibit a granular surface morphology. However, the mean grain size increases with seed layer thickness, reflecting improved grain coalescence during sputtering. Specifically, the average grain sizes are approximately 20 ± 4 nm for 80 nm thickness, ~29 ± 7 nm for 125 nm, and reach ~34 ± 11 nm and ~36 ± 12 nm for 240 nm and 450 nm, respectively [44].

The thickness of a ZnO seed layer strongly affects its microstructural evolution. Thin layers may form discrete, isolated grains, leading to incomplete surface coverage and limited grain coalescence. As the layer thickness increases, grains have more opportunity to merge and form larger, continuous domains, improving overall surface uniformity.

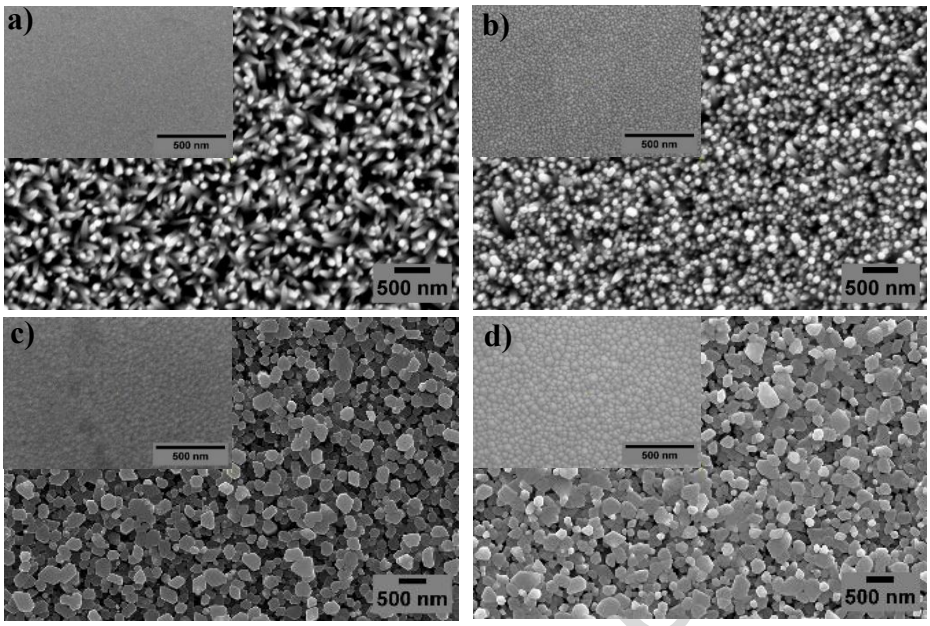

Figure 12: Top view SEM images of ZnO NWs synthesized for 14h on ZnO seed layers of thickness : (a) 80nm, (b) 125nm, (c) 240nm and (d) 450nm.

The top-view SEM images of NWs synthesized hydrothermally for 14 h on these seed layers reveal a strong correlation between seed layer thickness and NW morphology. On the 80 nm seed layer, NWs display irregular, pencil-like tips and poor vertical alignment, indicative of weak crystallographic guidance during growth. Similar characteristics still exist on the 125 nm layer, where a mixture of misaligned and moderately aligned NWs is observed.

In contrast, NWs synthesized on the 240 nm and 450 nm seed layers exhibit well-defined hexagonal terminations, uniform diameters, and excellent vertical alignment, confirming improved structure and alignment on thicker seed layers. Moreover, the lateral expansion of the NWs with increasing seed layer thickness leads to a reduction in NWs density, from about 200 ± 11 particles/μm^2 (on the 80 nm seed) to $\sim 36 \pm 8$ particles/μm^2 (on the 240 nm seed), as larger NWs diameters limit their number that can nucleate per unit area.

Table 3 provides a summary of the average grain sizes for ZnO seed layers and particle densities for ZnO NWs with different thicknesses (80 nm, 125 nm, 240 nm, and 450 nm), highlighting how increasing thickness influences the morphology, the orientation and the alignment of NWs growth and the reduction in surface particle density.

Table 3: Summary of seed layers grain sizes and NWs morphology, orientation, alignment and densities characteristics for each seed layer thickness.

Seed Layer Thickness (nm)	Mean Grain Size (nm)	NWs Tip Morphology	NWs Orientation	NWs Alignment	NWs Density (NWs/μm²)
80	~20 ± 4	Pencil-like ends	Random	Poor	200 ± 11
125	~29 ± 7	Pencil-like and hexagonal ends	Mixed (random + vertical)	Moderate	88 ± 13
240	~34 ± 11	Hexagonal facets	Vertical	Good	36 ± 8
450	~36 ± 12	Hexagonal facets	Vertical	Good	36 ± 6

Since the 240 nm and 450 nm seed layers both offer an optimal balance of ZnO NWs alignment, surface density, and morphological uniformity, the sample with NWs synthesized for 14 h on the 240 nm seed layer was selected as the most suitable substrate for further electrical and piezoelectric characterizations. This choice was motivated by the fact that the 240 nm seed layer represents the thinnest seed layer that still ensures excellent NWs orientation and structural consistency.

To further confirm the chemical composition and purity of the ZnO NWs synthesized on the 240 nm seed layer for 14 h, EDS analysis was performed.

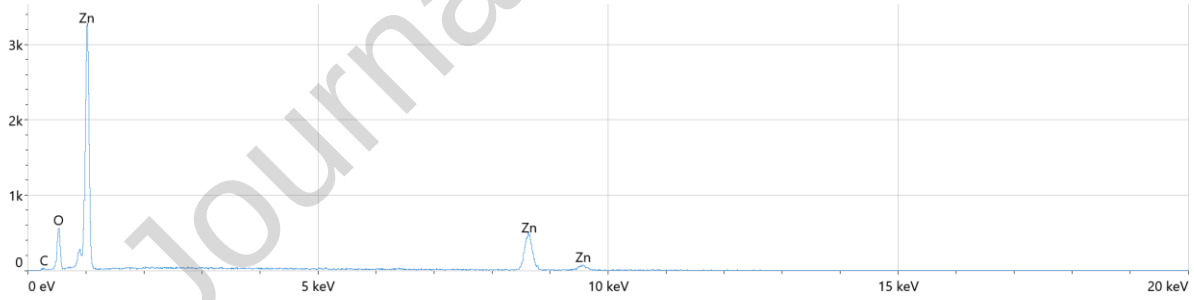

Figure 13: EDS Spectrum of ZnO NWs Synthesized on a 240 nm Seed Layer for 14 h.

The EDS spectrum (Figure 13) reveals three main characteristic peaks corresponding to zinc (Zn), oxygen (O), and carbon (C). The most intense peaks are attributed to Zn, located around 1 keV, 8.6 keV, and 9.6 keV, confirming that zinc is the dominant element in the nanostructure. A notable peak at approximately 0.5 keV is associated with oxygen, indicating the presence of significant oxygen content, as expected for ZnO. A minor peak at around 0.28 keV corresponds to carbon, which is likely due to surface contamination from environmental exposure during sample handling.

Quantitative analysis shows an atomic composition of approximately 51.8% Zn, 46.2% O, and only 2.0% C, suggesting that the NWs are nearly stoichiometric and of high chemical purity [45]. These results confirm the successful formation of ZnO NWs with minimal contamination, validating the

quality of the selected growth conditions for subsequent electrical and piezoelectric characterizations.

4.3. Electrical and piezoelectric properties

In this section, we investigate the electrical and piezoelectric properties of 240 nm-thick seed layer and 14h-synthesis NWs (figure 14). The NWs possess an average diameter of approximately 170 nm and a length of about 2 μm.

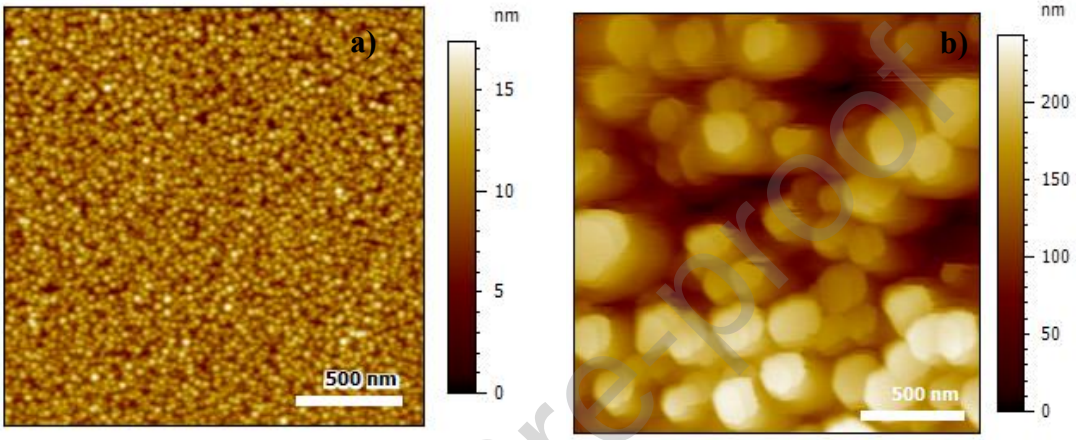

Figure 14: Topologies of : (a) 240 nm ZnO seed layer and (b) NWs synthesized for 14h performed with PFM.

The seed layer (240 nm thick) was deposited on a (001)-oriented silicon substrate pre-coated with a 100 nm Ti/Pt layer acting as a bottom electrode to enable electrical contact (Figure 15). For nanoscale electrical and piezoelectric characterizations, C-AFM and PFM were employed. A Pt/Ir-coated conductive AFM tip (SCM-PIT V2) served as the top electrode, enabling localized measurements of current flow and electromechanical response.

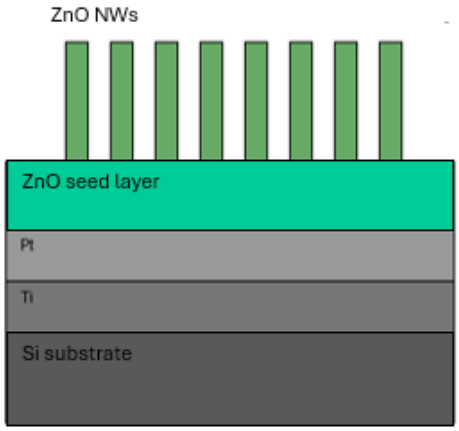

Figure 15: Schematic representation of hydrothermal synthesis of ZnO NWs on ZnO seed layer.

4.3.1. Electrical properties

Figure 16 presents the I–V characteristics obtained through C-AFM measurements of a bare Si, a 240 nm-thick ZnO seed layer sputtered under an (80:20)% Ar:O_2 gas mixture and ZnO NWs synthesized for 14 h on top of this seed layer. These measurements were performed by sweeping the DC bias from –10 V to +10 V.

The bare silicon substrate (Figure 16a) is electrically connected to the conductive AFM sample holder of the Bruker Dimension ICON, which acts as the bottom electrode. The top electrode is the SCM-PIT V2 conductive AFM tip. The measured current–voltage (I–V) characteristics exhibit a linear and symmetric behavior, indicating the formation of an ohmic contact between the AFM tip and the silicon surface. The nanoscale contact area combined with the force applied by the AFM tip enhances local electric fields and improves carrier transport across the interface. Consequently, the contact behaves as ohmic rather than rectifying.

The ZnO seed layer (Figure 16b) exhibits a nonlinear and asymmetric I–V behaviour, indicating a diode-like rectifying effect in their I-V response, similar to a Schottky diode, where current flows more easily in one direction than the other [46]. The leakage current remains relatively low (±1,5 nA) throughout the voltage sweep, and the turn-on voltage is observed around 3 V.

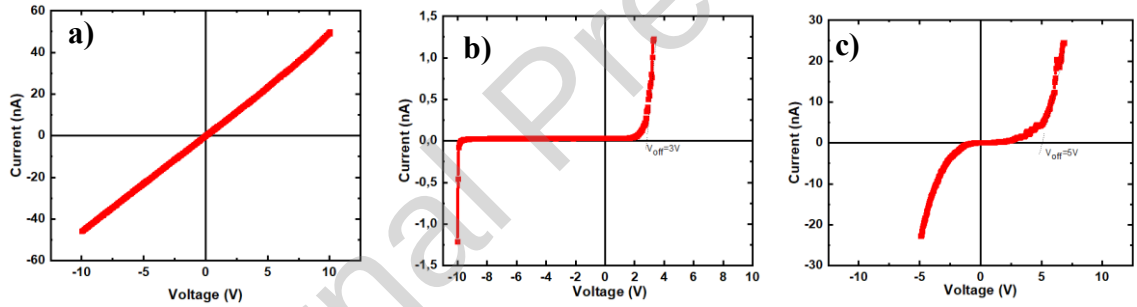

Figure 16: Current–voltage (I–V) characteristics of: (a) bare Si, (b) 240 nm ZnO seed layer and (c) NWs synthesized for 14 h, measured by C-AFM.

In contrast, the ZnO NWs synthesized for 14 h on the same 240 nm-thick seed layer (Figure 16c) exhibit higher current conduction, reaching approximately ±30 nA under ±10 V bias (about 20 times higher than the seed layer), with a turn-on voltage around 5 V. Like the seed layer, the I–V curve maintains a nonlinear, asymmetric behaviour, reinforcing the presence of a Schottky-like junction at the tip–NWs interface.

Comparing both curves (Figure 16b et c), the low current of ZnO seed layer can be attributed to the high resistivity and planar structure of the seed layer, which contains fewer surface defects and grain boundaries compared to vertically synthesized nanostructures. However, by growing a vertically aligned ZnO NWs on the seed layer, the current output is increased, which can be explained by the enhanced surface-to-volume ratio which increases surface defects (such as oxygen vacancies and interstitial zinc) [47] and also by improved electron transport [48].

In the context of sensing applications and piezoelectric performance, Schottky-type characteristics refer to the rectifying behavior that arises at the interface between a metal and a semiconductor. This behavior results from the formation of a potential barrier (Schottky barrier), which induces a

depletion region within the semiconductor and leads to preferential charge transport in a single direction.

This interface plays a decisive role in charge carrier transport mechanisms, electrical signal detection, and the overall efficiency of the device. When a piezoelectric material is subjected to mechanical stress, polarization occurs and generates bound charges at its surface. The presence of a Schottky contact makes it possible to modulate the collection and flow of these charges by limiting their recombination or screening by free carriers, in contrast to an ohmic contact.

In sensing devices, the rectifying nature of the Schottky contact contributes to a reduction in leakage currents and to an improvement in the signal-to-noise ratio, resulting in enhanced sensitivity to weak mechanical stimuli (pressure, vibration, deformation). The Schottky barrier thus acts as an active element of the sensor, efficiently converting the mechanical response into a usable electrical signal.

From the standpoint of piezoelectric performance and energy harvesting, Schottky characteristics help preserve the induced piezoelectric potential by preventing the immediate flow of charges that would otherwise cancel the internal electric field. This preservation of the electric field leads to an increase in the output voltage.

In summary, Schottky characteristics constitute an essential lever for controlling charge flow, optimizing the delivered voltage and power, and improving the reliability and efficiency of sensors and piezoelectric energy-harvesting devices.

4.3.2. Piezoelectric properties

The investigation of the effective piezoelectric response ($d_{33,eff}$) of the ZnO seed layer and NWs (figure 17) was preceded by system calibration (as described in the Characterizations section). After calibration and setup, PFM measurements were performed on the same samples used for the electrical tests.

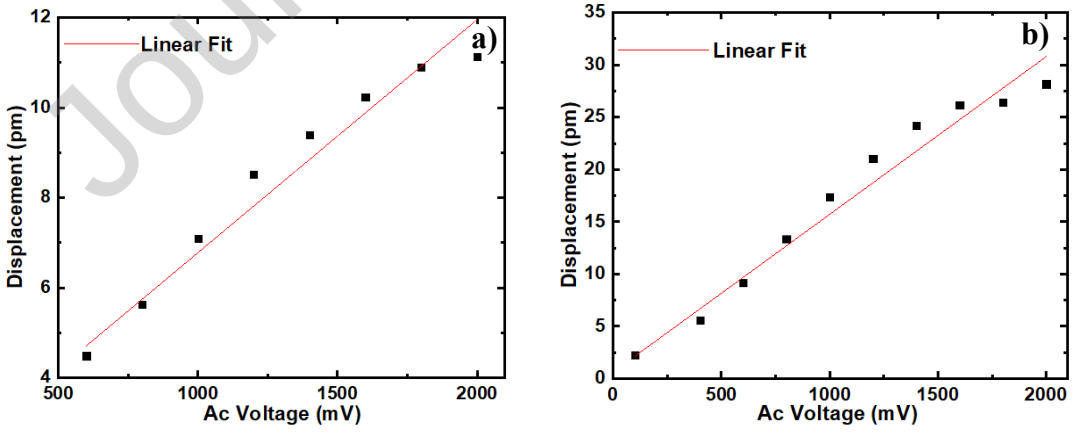

Figure 17: PFM measurements of (a) 240 nm ZnO seed layer and (b) NWs synthesized for 14h, as a function of applied AC Voltage..

Figure 17a shows that the 240 nm ZnO seed layer exhibits a linear nanoscale displacement response under AC bias, with an effective piezoelectric constant $d_{33,eff} \approx 5.2$ pm/V. In contrast, ZnO NWs

synthesized for 14 h on the same seed layer (figure 17b) show a much larger electromechanical response of about $d_{33,eff} \approx 15$ pm/V (nearly three times higher). This enhancement is attributed to the NWs' high aspect ratio (length-to-diameter), and the resulting geometric flexibility, which allow greater elastic deformation. In essence, the free-standing, vertically aligned NWs can more easily bend or elongate under bias compared to the seed layer, enabling more strain to develop and thus a higher Piezoresponse [49]. Another parameter is related to the quality of the contact between the AFM tip and the top surface of ZnO NW, which is impacting the distribution of electric field inside the NW, and therefore its piezo-response.

Likewise, experimental studies measuring the piezoelectric coefficient d_{33} have confirmed that ZnO nanostructures can exhibit enhanced effective piezoelectric responses. For instance, Scrymgeour *et al.* reported an effective piezoelectric coefficient d_{33},eff of approximately 9.5 pm/V for ZnO nanorods [50]. Legardinier *et al.* demonstrated d_{33},eff values ranging from 4.5 to 6.6 pm/V, depending on post-growth treatments [51]. In contrast, the highest mean piezoelectric coefficient measured by Quang *et al.* for ZnO nanowire arrays is about 3.7 pm/V [52]. Table 4 summarizes the effective piezoelectric coefficient ($d_{33,eff}$) of ZnO films and nanowires from this work, compared with the state of the art, all measured by PFM.

Table 4: Summary of the piezoelectric coefficient ($d_{33,eff}$) of ZnO films and nanowires.

ZnO film/NWs	d33 (pm/V)	References
Film	5,2	This work
	5-5,3	[53]
NWs	15	This work
	4,5-6,6	[51]
	3,7	[52]

However, it is important to note that the effective piezoelectric coefficients extracted from Piezoresponse force microscopy (PFM), which probes the inverse piezoelectric effect at the nanoscale, should be interpreted with caution. The PFM signal can be significantly influenced or amplified by elastic deformation, electrostatic effect, electrochemical strain, and local charge accumulation at the tip–sample interface [54], leading to an overestimation of the intrinsic piezoelectric response. Consequently, the $d_{33,eff}$ values obtained by PFM do not always directly reflect the true piezoelectric coefficient of the material.

For this reason, the reliability of PFM-derived piezoelectric coefficients must be validated through complementary approaches, including measurements based on the direct piezoelectric effect and macroscopic characterization techniques. Direct piezoelectric measurements under applied mechanical stress, as well as macroscopic electrical output measurements on devices or large-area samples, provide a more realistic assessment of the functional piezoelectric performance relevant to sensing and energy harvesting applications.

Conclusion

This study demonstrates the successful growth of vertically aligned ZnO NWs on optimized sputtered ZnO seed layers and highlights the critical parameters that govern their performance. By optimizing the RF sputtering conditions (specifically an $Ar:O_2$ ratio of 80:20) for the seed layer, we obtained highly textured ZnO seed layers that promote the aligned growth of ZnO NWs. We found that introducing moderate oxygen during seed layer deposition significantly refines the grain structure and increases the nucleation site density, which in turn yields dense, well-aligned NWs. Increasing the seed layer thickness improved the crystallographic guidance for NWs growth, with a 240 nm-thick seed providing an optimal balance of grain coalescence and alignment while keeping the layer reasonably thin.

Hydrothermal synthesis studies have revealed that the NWs morphology highly dependent on synthesis duration. Short synthesis (1 to 4 h) produces very dense NWs with smaller diameters, while longer synthesis durations (≥14 h) allow NWs to thicken and reduce in number (per unit area) as a coarsening progresses. Beyond 14 h, lateral growth reaches saturation and NWs continue to elongate (reaching approximately 2.5 µm at 24 h) without a significant increase in diameter. It should be noted that NWs synthesized on a bare silicon substrate (without a seed layer) were randomly oriented and exhibited poor crystallinity, highlighting the essential role of the seed layer in orienting vertical growth and improving structural quality.

Nanoscale electrical and piezoelectric characterizations confirmed the superior functional properties of the optimized ZnO NWs. Consistent results were obtained at different locations and over repeated measurements. Conductive AFM measurements displayed a rectifying (Schottky-like) I–V behaviour for seed layer and NWs. It showed that NWs exhibit higher current compared to the seed layer under the same bias that can be explained by the enhanced surface-to-volume ratio and charge transport. PFM measurements further revealed that the effective piezoelectric coefficient $d_{33,eff}$ of the ZnO NWs array is three times greater than that of the seed layer. This enhancement is attributed to the flexibility of the high-aspect-ratio NWs, which can undergo larger mechanical deformations under an electric field.

Several deposition runs and repeated characterizations carried out under identical experimental conditions consistently preserved the intrinsic structural, electrical, and piezoelectric properties of the material. The negligible variation observed from run to run highlights the high reproducibility and process stability of the fabrication protocol. This consistency strongly suggests good material durability and reliability, confirming that the optimized growth conditions enable stable performance over multiple synthesis cycles without degradation or aging effects.

Overall, the lead-free, eco-friendly, hydrothermally synthesized ZnO NWs optimized in this work exhibit excellent crystallinity, alignment, and enhanced electromechanical responses. These characteristics make them promising candidates for next-generation nano-sensors, piezoelectric nanogenerators, and other nano-electronic devices. Nevertheless, further investigations involving the fabrication and in-depth characterization of a device based on a nanowire network are necessary to validate its practical performance in real sensing and energy-harvesting applications.

As part of our future work, we plan to investigate the effect of doping ZnO nanowires to further enhance their piezoelectric performance. Among the trivalent dopants investigated, yttrium (Y^{3+}) has attracted significant attention. It has been shown to significantly improve ZnO's functional properties, increasing the d_{33} coefficient and inducing ferroelectric-like behavior. For instance, in

co-sputtered ZnO thin films, 1.6 at.% Y doping raised d_{33} from 12.4 pm/V to ~49.6 pm/V and produced a remanent polarization of ~0.04 μC/cm² [55]. Exceptional piezoelectric responses (~420 pm/V) have also been reported in Y-doped ZnO nanosheets [56], confirming the strong potential of yttrium doping for advanced piezoelectric nanodevices.

Acknowledgments

The authors would like to acknowledge the platform FUMAP at IEMN and LPNE Laboratory for providing the facilities necessary for conducting the research.

The authors thank also Université Polytechnique Hauts de France under EUNICE Alliance Program Grant (AAP PS 2022), CRECH (Umons) and FRS-FNRS for financing this work.

References

[1] V. Consonni and A. M. Lord, "Polarity in ZnO nanowires: A critical issue for piezotronic and piezoelectric devices," *Nano Energy,* 2021.

[2] T. Jalabert, M. Pusty, M. Mouis and G. Ardila, "Investigation of the diameter-dependent piezoelectric response of semiconducting ZnO nanowires by Piezoresponse Force Microscopy and FEM simulations," *Nanotechnology,* 2023.

[3] Z. L. Wang, "Zinc oxide nanostructures: Growth, properties and applications," *Journal pf Physics: Condensed Matter,* 2004.

[4] L. Yang, "Characterization of ZnO thin films prepared by direct current (DC) magnetron sputtering," 2012.

[5] B. Kiliç, L. Wang, O. Ozdemir, M. Lu and S. Tuzemen, "One-Dimensional (1D) ZnO Nanowires Dye Sensitized Solar Cell," *Journal of Nanoscience and NanotechnologY,* 2013.

[6] Z. Min, Z. Min, C. Ling, W. Haoming, Y. Xiaopeng and C. Bingqiang, "ZnO photoanodes with different morphologies grown by electrochemical deposition and their dye-sensitized solar cell properties," *Ceramics International,* 2014.

[7] V. Galstyan, E. Comini, A. Ponzoni, V. Sberveglieri and G. Sberveglieri, "ZnO Quasi-1D Nanostructures: Synthesis, Modeling, and Properties for Applications in Conductometric chemical sensors," *Chemosensors,* 2016.

[8] Y. R. and S. B., "Growth mechanism of hexagonal ZnO nanocrystals and their sensing application," *Materials Letters,* 2015.

[9] V. Gaddam, S. Joshi and M. Parmar, "A novel piezoelectric ZnO nanogenerator on flexible metal alloy substrate," *IEEE,* 2012.

[10] F. Anang, A. D. Refino, G. Harm, D. Li, J. Xu, M. Cain, U. Brand, Z. Li, M. Görke, G. Garnweitner and E. Peiner, "Thermo-Convective Solution Growth of Vertically Aligned Zinc Oxide Nanowire Arrays for Piezoelectric Energy Harvesting," *Micromachines,* 2024.

[11] X. Chen, A. M. C. Ng, K. K. Wong, A. B. Djurisic, F. Fang, W. K. Chan, W. Fong, H. F. Lui and C. Surya, "ZnO nanorods for light-emitting diode applications," *Proceedings of SPIE,* 2011.

[12] Z. Zhang, J. Du, B. Li, S. Zhang, M. Hong, X. Zhang, Q. Liao and Y. Zhang, "Ultrathin strain-gated field effect transistor based on In-doped ZnO nanobelts," *APL Materials,* 2017.

[13] O. E. Cigarroa-Mayorga, "Enhancement of photocatalytic activity in ZnO NWs array due to Fe_2O_3 NPs electrodeposited on the nanowires surface: The role of ZnO-Fe_2O_3 interface," *Materials Today Communications,* 2022.

[14] G. Zhu, Y. Zhou, S. Wang, R. Yang, Y. Ding, X. Wang, Y. Bando and Z. l. Wang, "Synthesis of vertically aligned ultra-long ZnO nanowires on heterogeneous substrates with catalyst at the root," *Nanotechnology,* 2012.

[15] F. Falyouni, L. Benmamas, C. Thiandoume, J. Barjon, A. Lusson, P. Galtier and V. Sallet, "Metal organic chemical vapor deposition growth and luminescence of ZnO micro- and nanowires," *Journal of Vacuum Science and Technology B,* 2009.

[16] M. T. Htay, Y. Hashimoto, N. Momose and K. Ito, "Position-selective growth of ZnO nanowires by ultrasonic spray pyrolysis," *Journal of Crystal Growth,* 2009.

[17] S. Inguva, R. K. Vijayaraghavan, E. McGlynn and J.-P. Mosnier, "High quality interconnected core/shell ZnO nanorod architectures grown by pulsed laser deposition on ZnO-seeded Si substrates," *Superlattices and Microstructures,* 2017.

[18] S. Käbisch, M. Timpel, H. Kirmse, M. A. Gluba, N. Koch and N. H. Nickel, "Polarity of pulsed laser deposited ZnO nanostructures," *Applied Physics Letters,* 2016.

[19] A. F. Abdulrahman, S. M. Ahmed, A. A. Barzinjy, S. M. Hamad, N. M. Ahmed and M. A. Almessiere, "Fabrication and Characterization of High-Quality UV Photodetectors Based ZnO Nanorods Using Traditional and Modified Chemical Bath Deposition Methods," *Nanomaterials,* 2021.

[20] N. B. Moussa, M. Lajnef, J. Chaste, R. Chtourou and E. Herth, "Highly C-oriented (002) plane ZnO nanowires synthesis," *RSC Advances,* 2023.

[21] M. C. Sigallon, A. Baillard, V. Consonni, F. Aubrit, N. Potrzebowska, R. Grasset, M. Tebellout, N. Gogneau, E. Sarrey, J.-E. Wegrowe and M.-C. Clochard, "Flexible piezoelectric energy harvester made of vertically-aligned ZnO nanowires hydrothermally-grown by template-assisted synthesis in poled PVDF," *Nano Trends,* vol. 10, p. 14, 2025.

[22] X. Jiang, J. Hao, P. Liu, Q. Gao, J. Yang and L. Liu, "Piezoelectric properties of ZnO nanowire arrays/DAST-PDMS flexible nanogenerators," *Applied Physics Letters,* vol. 123, p. 12, 2023.

[23] A. Pimentel, S. H. Ferreira, D. Nunes, T. Calmeiro, R. Martins and E. Fortunato, "Microwave Synthesized ZnO Nanorod Arrays for UV Sensors: A Seed Layer Annealing Temperature Study," *Materials,* vol. 9, no. 4, p. 15, 2016.

[24] F. E. B. Anang, M. Cain, M. Xu, Z. Li, U. Brand, D. Jangid, S. Seibert, C. Schwalb and E. Peiner, "Nondestructive Mechanical and Electrical Characterization of Piezoelectric Zinc Oxide Nanowires for Energy Harvesting," *Micromachines,* vol. 16, no. 8, 2025.

[25] A. Kerasidou, A. Bardakas, M. Botzakaki, S. Georga, C. Krontiras, K. Mergia, V. Psycharis and C. Tsamis, "Growth of ZnO nanowires on seeding layers deposited by ALD: Influence of process parameters," *Microelectronic Engineering,* 2019.

[26] Q. Liang, F. Qiao, X. Cui and X. Hou, "Controlling the morphology of ZnO structures via low temperature hydrothermal method and their optoelectronic application," *Materials Science in Semiconductor Processing,* 2019.

[27] L. Vayssieres, "Growth of arrayed nanorods and nanowires of ZnO from aqueous solutions," *Adv. Mater.,* 2003.

[28] H. Ghayour, H. Rezaie, S. Mirdamadi and A. A. Nourbakhsh, "The effect of seed layer thickness on alignment and morphology of ZnO nanorods," *Vacuum,* 2011.

[29] G. Kenanakis, D. Vernardou, E. Koudoumas and N. Katsarakis, "Growth of c-axis oriented ZnO nanowires from aqueous solution: the decisive role of a seed layer for controlling the wires' diameter," *Journal of Crystal Growth,* 2009.

[30] Y. Zhang, M. K. Ram, E. K. Stefanakos and D. Y. Goswami, "Synthesis, characterization, and applications of ZnO nanowires," *Journal of Nanomaterials,* 2012.

[31] A. Hamdi, A. Hamieh, M. Alamri, K. Dogheche, S. M. M.M., R. Desfeux, D. Remiens and E. Dogheche, "Morphological, structural, electrical, and piezoelectric analysis of hydrothermally grown ZnO nanowires on various substrates," *Surfaces and Interfaces,* 2022.

[32] T. Demes, Thomas, C. Ternon, D. Riassetto, V. Stambouli and M. Langlet, "Comprehensive study of hydrothermally grown ZnO nanowires," *Journal of materials science,* 2016.

[33] Anca-Danciu, V. Musat, T. Busani, J. V. Pinto, R. Barros, A. M. Rego, A. M. Ferraria, P. A. Carvalho, R. Martins and E. Fortunato, "Uniform Arrays of ZnO 1D Nanostructures Grown on Al:ZnO Seeds Layers by Hydrothermal Method," *Journal of nanoscience and nanotechnology,* vol. 13, no. 10, p. 10.

[34] P. Gerber, C. Kugeler, U. Bottger and R. Waser, "Effects of ferroelectric switching on the piezoelectric small-signal response (d_{33}) and electrostriction (M_{33}) of lead zirconate titanate thin films," *Journal of Applied Physics,* 2004.

[35] B. Zhou, A. V. Rogachev, Z. Liu, D. G. Piliptsou, H. Ji and X. Jiang, "Effects of oxygen/argon ratio and annealing on structural and optical properties of ZnO thin films," *Applied Surface Science,* 2012.

[36] B. A. Johan, M. M. Ali, M. J. Haque, M. H. Kabir and S. Roy, "An approach to investigate the structural, morphological, and optical properties of spray pyrolyzed B and Mg co-doped ZnO thin films," *Results in Materials,* vol. 19, p. 8, 2023.

[37] A. R. Galaly, A. Awad and A. A. Aboud, “From glass to cobalt oxide: investigating ZnO thin film characteristics,” *IOP Publishing,* vol. 100, no. 6, 2025.

[38] R. Aljarrah and I. M. Alessa, “The effect of annealing temperature on the structural and optical properties of nanostructure ZnO,” *INTERNATIONAL JOURNAL OF ENERGY AND ENVIRONMENT,* p. 6, 2019.

[39] R. Manoranjitham, P. S. P. Reddy, S. S. Kavi, S. De, E. R. Kumar, C. Srinivas, H. Ramalingam and A. A. El-Rehim, “Natural fuel assisted biogenic synthesis of ZnO nanoparticles: Evaluation of crystallite size, optical band gap and gas sensing ability,” *Journal of Alloys and compounds,* vol. 1018, 2025.

[40] E. Alfonso, J. Olaya and G. Cubillos, “Thin film growth through sputtering technique and its applications,” *Crystallization - Science and Technology,* 2012.

[41] S. Chen and J. Wu, “Nucleation mechanisms and their influences on characteristics of ZnO nanorod arrays prepared by a hydrothermal method,” *Acta Mater.*, 2011.

[42] R. Idiawati, N. Mufti, A. Taufiq, H. Wisodo, I. K. R. Laila, A. Fuad and S. Sunaryono, “Effect of growth time on the characteristics of ZnO nanorods,” *IOP Conference Series Materials Science Engineering,* 2017.

[43] N. A. Alshehri, A. R. Lewis, C. Pleydell-Pearce and T. G. Maffeis, “Investigation of the growth parameters of hydrothermal ZnO nanowires for scale up applications,” *Journal of Saudi Chemical Society,* 2018.

[44] S. Pokai, P. Limnonthakul, M. Horprathum, P. Eiamchai, V. Pattantsetakul, S. Limwichean, N. Nuntawong, S. Porntheeraphat and C. Chitichoypanya, “Influence of seed layer thickness on well-aligned ZnO nanorods via hydrothermal method,” *Materials Today: Proceedings,* 2017.

[45] S. H. Mohamed, “Synthesis, structural and ellipsometric evaluation of oxygen-deficient and nearly stoichiometric zinc oxide and indium oxide nanowires/nanoparticules,” *Pholosophical Magazine,* vol. 91, no. 27, p. 15, 2011.

[46] G. D. J. Smit, S. Rogge and T. M. Klapwijk, “Scaling of nano-Schottky-diodes,” *Applied Physics Letters,* 2002.

[47] E. Broitman, C. Bojorge, V. K. F. Elhordoy, G. Z. Gadioli, R. Marotti, H. Canepa and E. Dalchiele, “Comparative study on the properties of ZnO nanowires and nanocrystalline thin films,” *Surface and coating technology,* 2012.

[48] M. Maddah, C. P. Unsworth, G. J. Gouws and N. O. Plank, “Synthesis of encapsulated ZnO nanowires provide low impedance alternatives for microelectrodes,” *PLOS One,* 2022.

[49] N. Bhadwal, R. B. Mrad and K. Behdinan, “Review of Zinc Oxide Piezoelectric Nanogenerators: Piezoelectric Properties, Composite Structures and Power Output,” *Sensors ,* 2023.

[50] D. A. Scrymgeour and J. W. Hsu, “Correlated Piezoelectric and Electrical Properties in Individual ZnO Nanorods,” *Nano Letters,* 2008.

[51] L. Legardinier, G. Ardila, I. Gérald, C. Jiménez, M. Weber, F. Donatini and V. Consonni, "Enhancement of the piezoelectric response of ZnO nanowires grown via PLI-MOCVD using post-deposition treatments through adjusted screening and surface effects," vol. 17, no. 17, p. 15, 2025.

[52] Q. C. Bui, V. Consonni, C. Jiménez, H. Roussel, X. Mescot, B. Salem and G. Ardila, "Correlation between the Dimensions and Piezoelectric Properties of ZnO Nanowires Grown by PLI-MOCVD with Different Flow Rates," vol. 3, no. 3, p. 16, 2023.

[53] M. Laurenti, S. Stassi, M. Lorenzoni, M. Fontana, G. Canavese, V. Cauda and C. Pirri, "Evaluation of the piezoelectric properties and voltage generation of flexible zinc oxide thin films," vol. 26, 2015.

[54] O. Kwon, D. Seol, H. Qiao and Y. Kim, "Recent Progress in the Nanoscale Evaluation of Piezoelectric and ferroelectric properties via scanning probe microscopy," *Advanced Science,* vol. 7, p. 15, 2020.

[55] L.-C. Cheng, S. Brahma, J.-L. Huang and C.-P. Liu, "Enhanced piezoelectric coefficient and the piezoelectric nanogenerator output performance in Y-doped ZnO thin films," *Materials science in semiconductor processing,* vol. 146, p. 8, 2022.

[56] N. Sinha, S. Goel, A. Joseph, H. Yadav, K. Batra, M. K. Gupta and B. Kumar, "Y-doped ZnO nanosheets: Gigantic piezoelectric response for an ultra-sensitive flexible piezoelectric nanogenerator," *Ceramics international,* vol. 44, p. 9, 2018.

Biographies

Imen Ben Khaled: PhD candidate in a doctoral program between the Université Polytechnique Hauts-de-France (UPHF, France) at the Institute of Electronics, Microelectronics and Nanotechnology (IEMN), and the University of Mons (UMONS, Belgium) in the Laboratory for Physics of Nanomaterials and Energy (LPNE).

Elhadj Dogheche: My thesis co-supervisor, Professor at the Université Polytechnique Hauts-de-France.

Philippe Leclère: My thesis co-supervisor, Professor at the University of Mons.

Declaration of Competing Interest

The authors declare that they have no known competing financial interests or personal relationships that could have appeared to influence the work reported in this paper.

Highlights

- Zinc oxide (ZnO) Nanowires (NWs)
- ZnO Seed layer
- Piezoelectric response of ZnO NWs
- ZnO hydrothermal synthesis
- Vertically aligned ZnO NWs

Graphical abstract